

Article

Systematic Study on the Synthesis and Magnetism Properties of Manganese Ferrite MnFe_2O_4 by an Oxidation Roasting Process

Shanshan Wen ^{1,2}, Bing Chen ^{1,2}, Junhong Zhang ^{1,2}, Wenlong Zhan ^{1,2} , Zhijun He ^{1,2,*} and Lihua Gao ^{1,2} 

¹ School of Materials and Metallurgy, University of Science and Technology Liaoning, Anshan 114051, China; 312025@ustl.edu.cn (S.W.); 322021@ustl.edu.cn (B.C.); zhangjunhong@ustl.edu.cn (J.Z.); zhanwenlong@ustl.edu.cn (W.Z.); gaolihua@ustl.edu.cn (L.G.)

² Key Laboratory for Chemical Metallurgy Engineering of Liaoning Province, University of Science and Technology Liaoning, Anshan 114051, China

* Correspondence: hezhijun@ustl.edu.cn

Abstract: A low-cost and high-efficiency solid reaction method has been reported as an effective technology to synthesize manganese ferrite MnFe_2O_4 with a spinel crystal structure. This work clarified the underlying reason for the influence mechanism of SiO_2 and Al_2O_3 on the synthesis of MnFe_2O_4 . Synthetic MnFe_2O_4 polyhedral microparticles with a saturated magnetization of 71.19 emu/g, a ratio of saturation magnetization to residual magnetization (M_s/M_r) of 0.062 and a coercivity (H_c) of 6.50 Oe were successfully obtained at an oxidation roasting temperature of 1100 °C for 60 min. The experimental results indicate that the tetrahedral Mn^{2+} ions and octahedral Mn^{3+} ions in the crystal structure of manganese ferrite MnFe_2O_4 were replaced by tetrahedral Si^{2+} ions and octahedral Al^{3+} ions from $(\text{Mn}^{2+})_x(\text{Fe}^{2+})_y(\text{Si}^{2+})_{1-x-y}[\text{Fe}^{3+}]_2\text{O}_4$ and $(\text{Mn}^{2+})[\text{Fe}^{3+}]_{2-x}[\text{Al}^{3+}]_x\text{O}_4$, respectively. In addition, hercynite $\text{Fe}_x\text{Mn}_{1-x}\text{Al}_2\text{O}_4$ with a spinel crystal structure and olivine $\text{Mn}_x\text{Fe}_{2-x}\text{SiO}_4$ with an orthorhombic crystal structure were partially formed in the synthesis of manganese ferrite MnFe_2O_4 , in which some Fe^{2+} ions were easily replaced by Mn^{2+} ions to form stable hercynite MnAl_2O_4 and olivine Mn_2SiO_4 in these crystal structures. The current research work provides comprehensive insights for synthesizing manganese ferrite MnFe_2O_4 and continuously advances its technical progress.

Keywords: manganese ferrite; solid phase reaction; oxidation roasting; formation mechanism



Citation: Wen, S.; Chen, B.; Zhang, J.; Zhan, W.; He, Z.; Gao, L. Systematic Study on the Synthesis and Magnetism Properties of Manganese Ferrite MnFe_2O_4 by an Oxidation Roasting Process. *Crystals* **2023**, *13*, 1509. <https://doi.org/10.3390/cryst13101509>

Academic Editor: Arcady Zhukov

Received: 18 September 2023

Revised: 13 October 2023

Accepted: 15 October 2023

Published: 17 October 2023



Copyright: © 2023 by the authors. Licensee MDPI, Basel, Switzerland. This article is an open access article distributed under the terms and conditions of the Creative Commons Attribution (CC BY) license (<https://creativecommons.org/licenses/by/4.0/>).

1. Introduction

Spinel-type manganese ferrite (MnFe_2O_4) combines the advantages of iron-based and manganese-based materials and has many excellent physical and chemical properties. Manganese ferrites have been used in microwave adsorption [1–3], biomedicine [4,5], magnetic recording materials [6], electrode materials [7] and environmental remediation [8,9]. In the MnFe_2O_4 mixed spinel structure, the metal cations Mn^{2+} and Fe^{3+} are distributed in the A (tetrahedral) and B (octahedral) positions, and the oxygen anions are formed by the face-centered densely packed $[\text{Mn}^{2+}_{1-i}\text{Fe}^{3+}_i]_{\text{A}}[\text{Mn}^{2+}_i\text{Fe}^{3+}_{2-i}]_{\text{B}}\text{O}_4$ [10–12], where i is the inversion parameter as a reference for the inversion degree. When the manganese cation is on the regular tetrahedron ($i = 0$), it is characterized as a normal spinel structure, and when the manganese cation is in the octahedron position ($i = 1$), it is characterized as an inverse spinel structure [10]. Due to their strong surface energy and magnetic properties, nanometer ferrite functional magnetic particles are extremely prone to aggregation during the preparation process [13]. To solve the problem of particle aggregation, researchers have used different techniques to synthesize ferrite functional materials, such as hydrometallurgical technologies [13–16], solid-state reaction methods [17–25], combined electrochemical and chemical methods [26,27] and combined pyro- and hydrometallurgical metallurgical technology [11,28,29].

By comparison with the above synthesis methods, hydrometallurgy and combined methods are reported for synthesizing high-purity manganese ferrites. However, the above-mentioned methods have high cost, high energy consumption and complex technology, which seriously restrict their development. Solid-state synthesis has been widely considered a cost-effective way to synthesize manganese ferrite [18,28,29]. As we all know, magnetism is an important index for characterizing manganese ferrite, and the purity of raw materials and preparation conditions will directly affect its magnetism. As studied by Lin et al. [15], MnFe_2O_4 with different morphologies was successfully synthesized by a solvothermal method using cetyltrimethylammonium bromide as the raw material, and the minimum coercivity was 11.9 Oe. Rashad et al. [23] successfully synthesized MnFe_2O_4 with a saturation magnetization of 27.24 emu/g by acid leaching with low-grade manganese ore at pH 10, a calcination temperature of 1000 °C and a calcination time of 120 min. Ahmed et al. [24] found that manganese ferrite with a maximum saturation magnetization of 62 emu/g was successfully synthesized by sintering for 2 h at 1300 °C using mill scale and fine particles of manganese ore sinter as the source of ferromanganese spinel. Ding et al. [25] showed that the maximum saturation magnetization of MnFe_2O_4 samples formed after annealing at 600–700 °C increased from 54 emu/g to 79 emu/g. Reddy et al. [22] performed spark plasma sintering (SPS) of the hydrothermally pretreated material to obtain a soft magnetic material MnFe_2O_4 with a maximum saturation magnetization of 82.5 emu/g. To date, much research has been carried out on the preparation of MnFe_2O_4 with the solid-phase reaction method [18,30,31], and the experiments have proven that the magnetic properties of manganese ferrite are closely related to the structure and morphology of the crystal [18–21]. Since the influence of SiO_2 as well as Al_2O_3 on the asynchronous reaction behavior and product properties of ferromanganese oxides in the solid-phase process is not clear, the study of silicon and aluminum elements is of great significance in elucidating their impact on the synthesis of manganese ferrite, providing theoretical support for the solid-state reaction method of preparing manganese ferrite from ferromanganese ore. The clarification of the interfacial reaction process and the control of the interfacial reaction products is one of the urgent problems in this field.

In this paper, high-purity manganese ferrite MnFe_2O_4 was prepared by a solid-reaction method in which the evolution of its phase transition, magnetic properties and morphological characteristics were investigated by scanning electron microscopy (SEM), energy dispersive X-ray spectroscopy (EDS), X-ray diffraction (XRD), vibrating sample magnetometer (VSM) and Mössbauer spectroscopy (MBS) analyses. Some impurity components have a certain impact on the synthesis process of MnFe_2O_4 . This work clarified the underlying reason for the influence mechanism of SiO_2 and Al_2O_3 on the synthesis of MnFe_2O_4 in SiO_2 - MnO - Fe_2O_3 systems and Al_2O_3 - MnO - Fe_2O_3 systems. Therefore, the phase formation and synthesis mechanism of SiO_2 - MnO - Fe_2O_3 systems and Al_2O_3 - MnO - Fe_2O_3 systems were also investigated by X-ray diffraction (XRD) and scanning electron microscopy (SEM) and energy dispersive X-ray spectroscopy (EDS) analysis. Based on these findings, the current research work provides comprehensive insights for synthesizing manganese ferrite MnFe_2O_4 and continuously advances its technical progress.

2. Materials and Methods

2.1. Raw Materials

The purity of the MnO , Fe_2O_3 , SiO_2 and Al_2O_3 raw materials used in this study was 99.9%, and the reagents were not further purified during the experiment. The gas used was compressed air with a purity of 99.9% or higher. The average particle sizes of the Fe_2O_3 , MnO , SiO_2 and Al_2O_3 purity reagent powders were 56.2 μm , 35.2 μm , 30.6 μm and 26.4 μm , respectively, using a Malvern laser particle size analyzer (Mastersizer 2000, Shanghai, China).

2.2. Synthesis Procedure

In this paper, three kinds of samples were used to assess oxidative competition behavior and synthesis mechanism in the synthesis process of manganese ferrite MnFe_2O_4 .

Sample A was Fe_2O_3 -MnO powder used to obtain optimized process parameters for this technology. Sample B was a mixture of pure SiO_2 , MnO and Fe_2O_3 powders used to clarify the effect of SiO_2 on the synthesis mechanism of MnFe_2O_4 . Finally, sample C was a mixture of pure MnO, Fe_2O_3 and Al_2O_3 powders used to elucidate the effect of Al_2O_3 on the synthesis mechanism of MnFe_2O_4 . Next, the prepared powder sample was mixed evenly by the ball star mixer for 2 h. Then, the mixed samples with diameters of 15 mm and heights of 20 mm were placed into cylindrical molds with briquette equipment operated at a pressure of 15 MPa. The briquettes were placed on a corundum substrate (size: 60 mm \times 60 mm) and roasted in air atmosphere to synthesize MnFe_2O_4 . The oxidation roasting temperature was also measured by a Pt-Rh thermocouple and controlled using a digital temperature controller (accuracy ± 1 °C). After the equipment reached the set temperature during roasting, the samples placed in a square corundum crucible were placed in the constant temperature zone of the furnace chamber, and at the same time, a mass flow rate of 2.0 dm^3/min was passed into the reaction equipment in air atmosphere. Then, following a certain time of oxidative roasting at the set temperature, the roasted product was placed in the cooling apparatus and cooled to room temperature at a cooling rate of 22 °C/min for subsequent characterization tests. In the same process as above, different mass fractions of SiO_2 and Al_2O_3 were added to the MnO- Fe_2O_3 system with a molar ratio of 1:1 by oxidative roasting, and the products were later used for characterization tests. Other detailed descriptions of the above equipment were reported in our previous studies [31].

2.3. Characterization Methods

The samples were cooled after oxidative roasting in a muffle furnace and ground with 200-mesh (<0.074 μm) fine particles. X-ray diffraction (XRD) was performed on the samples using RIGAKU D/Max 2500 with a scanning angle of 5°–85°, step size of 0.02° (2 θ) and scanning speed of 12°/min. The scanning results were analyzed using X'Pert HighScore Plus software 5.2 to assess the phase transformation and microstructure of the specimens.

The microscopic morphological characteristics of the intermediate products and the synthesized manganese ferrite particles were observed by scanning electron microscopy (SEM) and energy dispersive X-ray spectroscopy (EDS), and the interfacial reaction behaviors during the synthesis process were analyzed by point scanning and line scanning. The oxidation reaction behavior and formation mechanism of MnO and Fe_2O_3 powder were analyzed by a diffusion coupling model.

The magnetic properties of the synthesized manganese ferrite (MnFe_2O_4) particles were examined at room temperature using a JDAW-2000 C&D vibrating sample magnetometer (VSM). Since different magnetic materials have different magnetization properties, in considering the magnetic properties of the materials for comparison, the magnetic properties of the reaction samples will be compared by saturation magnetization intensity.

To further determine the occupancy of trivalent ferric ions in manganese ferrite, the experimental samples were analyzed by Mössbauer spectroscopy at room temperature. In the study of magnetic properties of solids, Mössbauer spectroscopy can be used to determine the magnetic ordering temperature, type of magnetic ordering and whether the ferromagnetic solid is antiferromagnetic or ferromagnetic. And this device can analyze the population of magnetic ions between various sublattices and study magnetic or spin structures. In the study of microcrystals, Mössbauer spectroscopy can provide information on the relaxation process of magnetic microcrystals, the number of magnetic anisotropy constants, the size and distribution of microcrystals and other aspects.

3. Results and Discussion

3.1. Discussion on the Oxidation Behavior of MnO- Fe_2O_3 System

3.1.1. Phase Transition and Synthesis Mechanism in MnO- Fe_2O_3 System

Figure 1 displays the XRD patterns of the MnO- Fe_2O_3 system oxidized and roasted at 900 to 1200 °C for 60 min. As shown in Figure 1a, the characteristic diffraction peaks

of Mn_2O_3 and Fe_2O_3 gradually decreased and disappeared. The oxidization roasting temperature increased from $900\text{ }^\circ\text{C}$ to $1000\text{ }^\circ\text{C}$. In this temperature range, the characteristic diffraction peak intensities of MnFe_2O_4 and $\text{Mn}_x\text{Fe}_{3-x}\text{O}_4$ increased, which indicated that Mn_2O_3 decomposed into MnO and Mn_3O_4 and then combined with Fe_3O_4 to form $\text{Mn}_x\text{Fe}_{3-x}\text{O}_4$. The diffraction peaks of Fe_2O_3 were not detected with increasing oxidization roasting temperature from $1000\text{ }^\circ\text{C}$ to $1100\text{ }^\circ\text{C}$. Nevertheless, the diffraction peak intensity of $\text{Mn}_x\text{Fe}_{3-x}\text{O}_4$ was enhanced and approached the standard diffraction peak of (2 2 0), which indicated that the purity and crystallinity of the synthesized MnFe_2O_4 increased with increasing roasting temperature. As observed in Figure 1b, the characteristic diffraction peak intensities of Fe_xO_4 and Fe_2O_3 were detected when the oxidization roasting temperature was below $1000\text{ }^\circ\text{C}$, while the intensity of the characteristic peak of MnFe_2O_4 showed an initial increasing trend followed by stabilization with increasing roasting temperature. In addition, the 2θ value of the diffraction peak (3 1 1) of $\text{Mn}_x\text{Fe}_{3-x}\text{O}_4$ ($1 \leq x \leq 2$) was 35.132° . These results demonstrated that the higher oxidization roasting temperature facilitated the synthesis of manganese ferrite, improved its crystal structure and optimized the atomic distribution in the crystal structure of spinel MnFe_2O_4 . Figure 1c displays the crystal structure of MnFe_2O_4 , which is able to verify the transformation of $\text{Mn}_x\text{Fe}_{3-x}\text{O}_4$ to MnFe_2O_4 in the mixture with increasing roasting temperature. In the MnFe_2O_4 mixed spinel structure, the metal cations Mn^{2+} and Fe^{3+} are distributed in the A (tetrahedral) and B (octahedral) positions, and the oxygen anions are formed by the face-centered densely packed $[\text{Mn}^{2+}_{1-i}\text{Fe}^{3+}_i]_{\text{A}}[\text{Mn}^{2+}_i\text{Fe}^{3+}_{2-i}]_{\text{B}}\text{O}_4$ [10–12]. The above analysis demonstrates that MnFe_2O_4 cannot be stabilized at lower stabilization temperatures. However, with increasing roasting temperature, the spinel manganese ferrite MnFe_2O_4 can exist stably. In addition, PDF standard card (MnFe_2O_4 , PDF#74-2403, cubic, Fd-3m (2 2 7), $8.511\text{ \AA} \times 8.511\text{ \AA} \times 8.511\text{ \AA}$) and then the XRD Rietveld refinement indicated that the synthesized MnFe_2O_4 had a cubic structure, and the cell parameter was $8.505\text{ \AA} \times 8.505\text{ \AA} \times 8.505\text{ \AA}$, which was close to the abovementioned PDF standard card for MnFe_2O_4 .

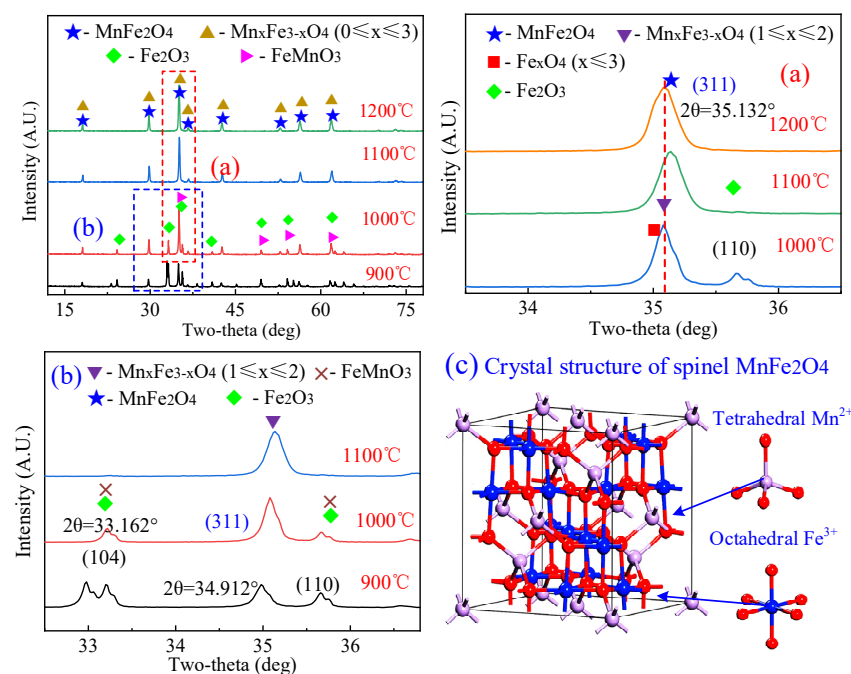


Figure 1. XRD patterns of the synthetic MnFe_2O_4 samples at a temperature from 900 to $1200\text{ }^\circ\text{C}$ with the atomic ratio of $\text{MnO}:\text{Fe}_2\text{O}_3 = 1:1$ for 60 min in air atmosphere and the crystal structure of spinel MnFe_2O_4 , (a) the oxidization roasting temperature of $900\text{ }^\circ\text{C}$ to $1200\text{ }^\circ\text{C}$, (b) Partial enlargement of Figure with two-theta range from 33.5° to 36.5° , (c) Partial enlargement of Figure with two-theta range from 32.5° to 36.7° , (c) Crystal structure of spinel MnFe_2O_4 .

Figure 2 illustrates the scanning electron micrographs of the cross-sectional layers of the synthesized manganese ferrite samples at 900 °C and 1100 °C for 60 min. Figure 2a clearly shows that the synthesized ferromanganese oxides have a regular polyhedral structure at a roasting temperature of 900 °C. From the overall appearance morphology, it can be seen that the polyhedral particles have obvious accumulation and gaps of different sizes exist. However, the sample particles have obvious boundaries. The corresponding energy spectrum scan lines reveal that the Mn, Fe and O contents in the sample are basically constant at a ratio of 1:1:3, indicating a relatively uniform distribution of the products. This result precisely coincides with the characteristic XRD peak at 900 °C in Figure 1. The cross-sectional SEM images of the sample roasted at 1100 °C for 60 min are shown in Figure 2b,c. The particles in the sample exhibit a flat spherical shape, and the gaps between the particles are relatively uniform with obvious boundaries. The energy spectrum analysis revealed that the average contents of integrated Mn, Fe and O were 13.67%, 26.51% and 59.83%, respectively, which were close to the theoretical values of the atomic ratio of pure MnFe_2O_4 . The Line 2 scan observed that the atomic ratios and contents of Mn, Fe and O were constant on individual particles, indicating that the distribution of these elements in the sample product was uniform. The experimental results do not correspond to the theoretical values due to the rapid oxidation rate of Mn^{2+} , and the related reasons can be further determined comprehensively by magnetic analysis.

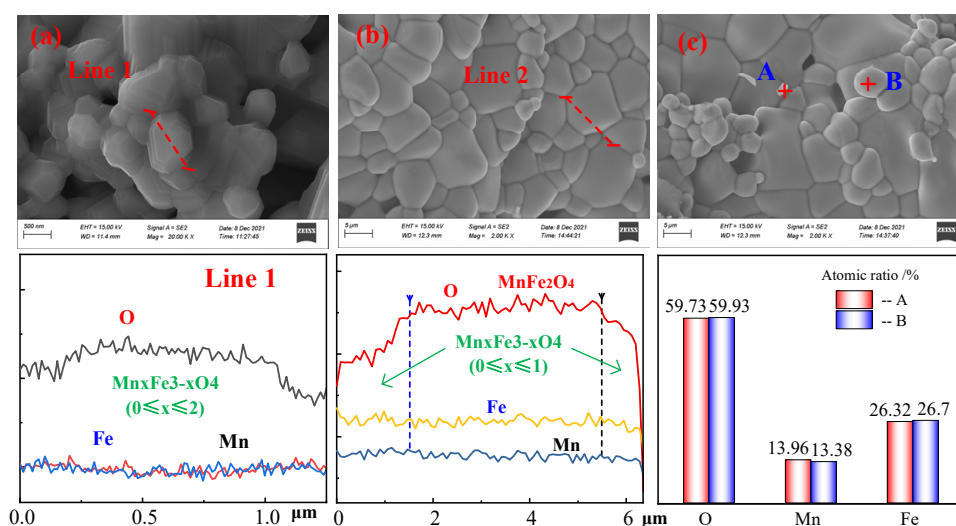


Figure 2. SEM-EDS micrograph of the surface layer in the section of the synthetic manganese ferrite samples in air atmosphere, for 60 min (a) Samples roasted at 900 °C (b) Samples roasted at 1000 °C and Samples roasted at 1100 °C. (c) The atomic ratios and contents of Mn, Fe and O on individual particles, A and B.

3.1.2. Magnetic Transformation

The magnetization hysteresis loops of the prepared $\text{Mn}_x\text{Fe}_{3-x}\text{O}_4$ products at 900–1200 °C were investigated with VSM, as illustrated in Figure 3. The saturation magnetization intensity M_s of the samples at different temperatures increased from 16.03 emu/g to 72.04 emu/g with increasing roasting temperature. The saturation magnetization intensity was 16.03 emu/g at 900 °C. The explanation for this result combined with Figure 3 shows that a large amount of MnFeO_3 could be generated from MnO and Fe_2O_3 at lower temperature, which leads to the decline of magnetism. Researchers have found that the saturation magnetization strength is proportional to the grain size of the magnetic material [24,32,33], and increasing the temperature will benefit the growth of $\text{Mn}_x\text{Fe}_{3-x}\text{O}_4$ [18,24]. In addition, the saturation magnetic strength of MnFe_2O_4 involves the distribution of cations on the A or B sites of the spinel crystal structure sites. Therefore, the variation pattern of M_s of manganese ferrite as affected by temperature is also attributed to the variation in Mn^{2+} or Fe^{2+} (Fe^{3+}) concentration

in the $Mn_xFe_{3-x}O_4$ sample. The coercivity (H_c) and the ratio of saturation magnetization intensity (M_s) to residual magnetization intensity (M_r) at room temperature and oxidation roasting temperature are shown in Figure 3. The hysteresis lines of the roasted samples show a narrow hysteresis behavior of the ferromagnetic material. As the roasting temperature increased from 900 °C to 1200 °C, the coercivity of the samples decreased from 30.3 Oe to 3.2 Oe, and M_s/M_r decreased from 0.121 to 0.051. The saturation magnetization intensity of the pure $MnFe_2O_4$ sample at 1100 °C was 71.8 emu/g [34] and 71.19 emu/g in this study. The crystalline particles of the samples are more complete, and the magnetic properties are closer to those of the pure $MnFe_2O_4$ sample, which has better magnetic properties.

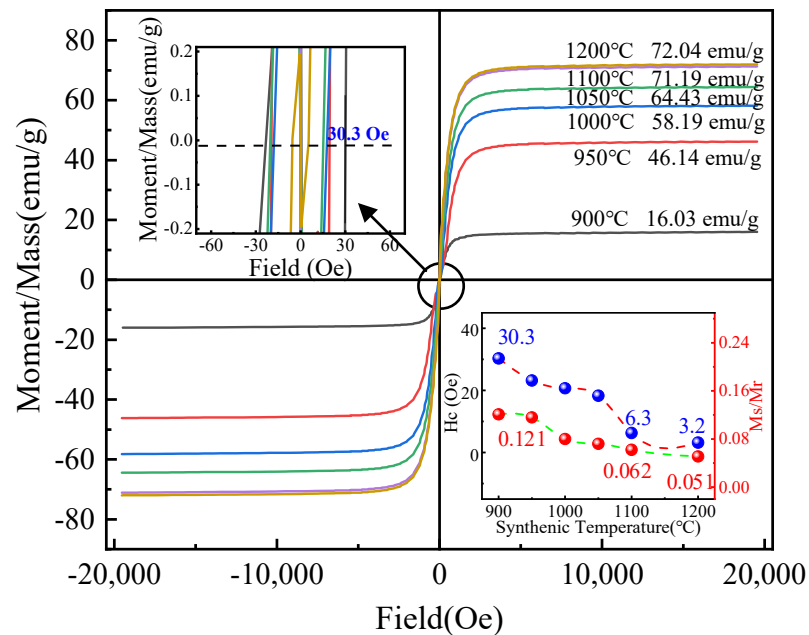


Figure 3. Magnetic hysteresis loops of $MnFe_2O_4$ samples roasted at temperatures in the range of 900 °C–1200 °C for 60 min in an air atmosphere.

3.1.3. Oxidative Competition Behavior of MnO - Fe_2O_3 System in Oxidation Roasting Process

X-ray photoelectron spectroscopy (XPS) was used to detect and assess the chemical states of Fe and Mn to clarify the oxidation behavior and consolidation mechanism of manganese ferrite $MnFe_2O_4$. The XPS spectra in the Fe 2P regions and Mn 2P regions are illustrated in Figure 4a,b. XPS data are systematically analyzed and evaluated through XPS database XPS Peak software 4.2. In the preparation process of $MnFe_2O_4$, the valuable metal ions could occupy the tetra-coordination and octa-coordination in the spinel crystal structure, resulting in different valence states of Fe cations (Fe^{2+} and Fe^{3+}) and Mn cations (Mn^{2+} and Mn^{3+}) for different binding energies of the Fe 2p electrons and Mn 2p electrons. In addition, the binding energies of the Fe $2p_{3/2}$ peaks for FeO, Fe_3O_4 and Fe_2O_3 appeared at 709.8 eV, 710.6 eV and 711.6 eV, respectively. The binding energies of the Mn $2p_{3/2}$ peaks for MnO, Mn_3O_4 and Mn_2O_3 appeared at 640.0 eV, 641.2 eV and 642.2 eV, respectively [34,35]. It was found that the intergrade area of $Fe2p_{3/2}$ for FeO at a binding energy of 709.8 eV gradually decreased and that of Fe_3O_4 at 710.6 eV also decreased, while that of Fe_2O_3 at 711.6 eV gradually increased with increasing oxidation roasting temperature from 900 °C to 1000 °C. In the meantime, the intergrade area of $Mn2p_{3/2}$ for MnO at a binding energy of 709.8 eV and Mn_3O_4 at a binding energy of 641.2 eV changed slightly, and that of Mn_2O_3 at a binding energy of 642.2 eV instantly decreased. These results showed that the higher temperature could effectively enhance the oxidation of Fe^{2+} ions in composite oxides to Fe^{3+} ions and improve the dissociation of Mn_2O_3 in the crystal spinel structure of $MnFe_2O_4$.

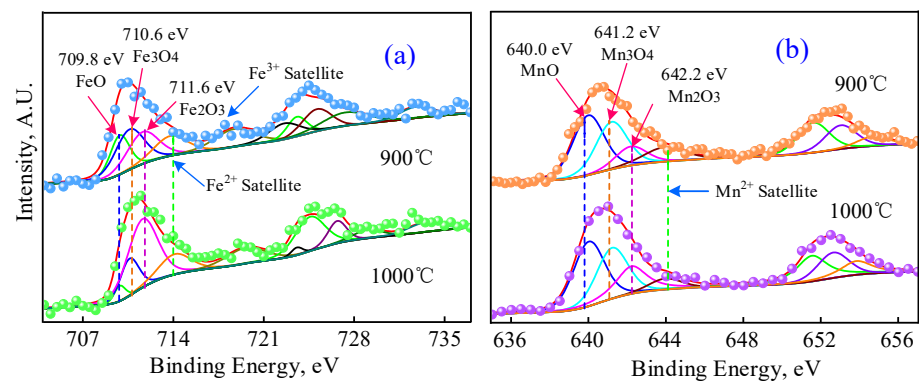


Figure 4. XPS spectra of the synthetic MnFe_2O_4 with (a) Spectra in Fe2p region and (b) Spectra in Mn2p region.

Figure 5a illustrates the element ratios on the reaction surface. In theory, the atomic ratios of Fe, Mn and O should be 14.29% 28.57% and 57.14%, respectively, in the crystal structure of MnFe_2O_4 . The error between the experimental data and the theoretical calculation value is small. However, there are differences in the occupancy of metal ions in the crystal structure of spinel manganese ferrite, which demonstrated that the vacancy oxygen in the crystal structure of $\text{Mn}_x\text{Fe}_{3-x}\text{O}_4$ was gradually filled to form lattice oxygen in the crystal structure of MnFe_2O_4 . The higher oxidation roasting temperature helps to adjust the atomic ordering of the spinel structure. Figure 5b illustrates the Mössbauer spectrum of the $\text{MnO-Fe}_2\text{O}_3$ system at different temperatures. The Mössbauer spectrum of each sample is clearly composed of asymmetric magnetic fine splitting hexagonal peaks. Moreover, each sample is superimposed with two different sets of characteristic diffraction peaks of spinel-type manganese ferrite, representing the Mössbauer spectra of the tetrahedral site (A-site) and octahedral site (B-site) [36,37]. Based on the characteristic that the oxygen atoms in the A-site are closer to the metal ions ($\approx 0.67 \text{ \AA}$) than in the B-site ($\approx 0.72 \text{ \AA}$), both the values of the homogeneous anomeric shift of Fe in the B-site are larger than those in the A-site. It is evident that the percentage of ortho-spinel increases in the shift from the A-site to the B-site as the roasting temperature of the sample is transformed from $900 \text{ }^\circ\text{C}$ to $1000 \text{ }^\circ\text{C}$, which demonstrated that the single bridging oxygen of tetra-coordination and hexa-coordination in composite oxides were transformed into the double bridging oxygen of hexa-coordination in the crystal spinel structure of MnFe_2O_4 under the action of high temperature.

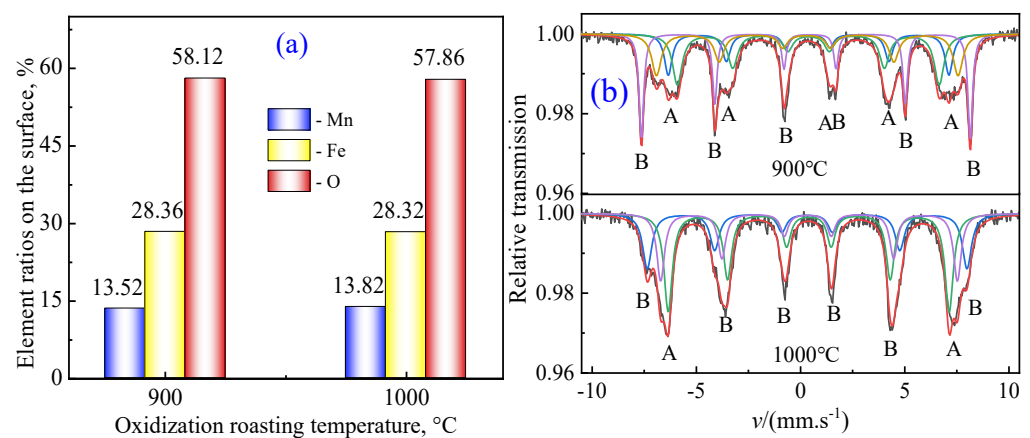


Figure 5. Element ratios on the surface (a) and Mössbauer spectrum (b) at different oxidation roasting temperature for 30 min in air atmosphere, A—tetrahedral site and B—octahedral site.

3.2. Discussion on the Oxidization Behavior of MnO-Fe₂O₃-SiO₂ System

Figure 6 illustrates the XRD patterns of the MnO-Fe₂O₃-SiO₂ system at temperatures from 900 to 1200 °C with different SiO₂ contents. The XRD patterns at different roasting temperatures from 900 °C to 1200 °C are shown in Figure 6a. The main phases detected are Mn₂O₃, Fe₂O₃, SiO₂ and a small amount of Mn_xFe_{3-x}O₄ at 900 °C, indicating that Mn₂O₃ and Fe₂O₃ are poorly synthesized Mn_xFe_{3-x}O₄ at lower temperatures. It can be seen from Figure 6a,b that the diffraction peaks of Mn₂O₃ and Fe₂O₃ disappear, the intensity of the characteristic peak of Mn_xFe_{3-x}O₄ constantly increases and the main diffraction peak approaches the main characteristic peak of MnFe₂O₄ (PDF#10-0319) with $2\theta = 34.981^\circ$ as the roasting temperature increases from 900 °C to 1100 °C. SiO₂ exists mainly as free SiO₂ and a very small amount of manganese-iron olivine phase (Mn_xFe_{1-x})₂SiO₄, corresponding to the card information (PDF#65-0466, $2\theta = 26.636^\circ$) in this temperature range. This demonstrated that the influence of SiO₂ on the oxidative roasting of the MnO-Fe₂O₃ system for the synthesis of MnFe₂O₄ is small when the roasting temperature is within 900–1100 °C. As the temperature increases to 1200 °C, the intensity of the characteristic peaks of SiO₂ and MnFe₂O₄ slightly decreases, while (Mn_xFe_{1-x})₂SiO₄ is relatively enhanced, indicating that the excessive temperature will force SiO₂ to react with some of the Fe and Mn oxides to form a small amount of manganese-iron olivine phase (Mn_xFe_{1-x})₂SiO₄. XRD patterns of SiO₂ with different contents were roasted at 1100 °C for 120 min in the MnO-Fe₂O₃ system. The intensity of the characteristic diffraction peaks of SiO₂ and (Mn_xFe_{1-x})₂SiO₄ in the product increased with increasing SiO₂ content, the intensity of the characteristic peak of MnFe₂O₄ decreased and then increased and the main characteristic peak shifted from $2\theta = 34.936^\circ$ to $2\theta = 35.022^\circ$. It can be inferred that the formation of (Mn_yFe_xSi_{1-x-y})Fe₂O₄ is related to both temperature and SiO₂ content. The formation of (Mn_yFe_xSi_{1-x-y})Fe₂O₄ mainly originated from Mn_xFe_{3-x}O₄, in which the tetrahedral Fe²⁺ ions in the crystal structure of Mn_xFe_{3-x}O₄ were replaced by tetrahedral Si²⁺ ions in the crystal structure of silicates to form (Mn_yFe_xSi_{1-x-y})Fe₂O₄ at higher oxidation roasting temperatures. Next, the tetrahedral Fe²⁺ ions and Si²⁺ ions in the crystal structure of (Fe_xSi_{1-x})Fe₂O₄ were replaced by tetrahedral Mn²⁺ and Fe²⁺ ions to form (Mn_yFe_xSi_{1-x-y})Fe₂O₄ ($0 < x + y < 1$) at higher oxidization roasting temperatures. The replaced Mn²⁺ ions and Fe²⁺ ions were combined with the replaced Si²⁺ ions to form Mn_xFe_{2-x}SiO₄ ($0 \leq x \leq 2$) by the oxidation roasting process. In summary, higher oxidization roasting temperatures are recommended for improving the recrystallization process of MnFe₂O₄.

Figure 7 shows the scanning electron micrographs of the cross-sectional layers of the MnO-Fe₂O₃-SiO₂ sample when roasted at 1100 °C for 120 min. The sample cross-section was found to have an irregular polyhedral structure and pores of different sizes, whereas there were obvious boundaries between individual particles and obvious precipitates at the edges of individual particles. Figure 7a presents the results of the line-scan energy spectrum, which shows that the content of Mn, Fe and O in the precipitates is close to 1:2:4, while the content of Si is almost nonexistent. This shows that Si cannot enter the crystal lattice of MnFe₂O₄ and that SiO₂ does not react with the MnO-Fe₂O₃ system under the experimental conditions. The reason for the presence of free SiO₂ in Figure 5 was further verified. The results of Figure 7b were obtained by energy spectrum scanning of points A and B. The apparent Si to O atomic ratio was approximately 1:2, which again verified that SiO₂ exists in the free state and that its morphology is obviously different from that of manganese ferrite. Combined with the presence of Si in the XRD spectrum of Figure 6, it can be inferred that free SiO₂ and (Mn_xFe_{1-x})₂SiO₄ are mainly attached to the surface layer of the product and have similar polyhedral structures. The presence of SiO₂ mainly affects the microstructure of manganese ferrite compared with the SEM image of the MnO-Fe₂O₃ system.

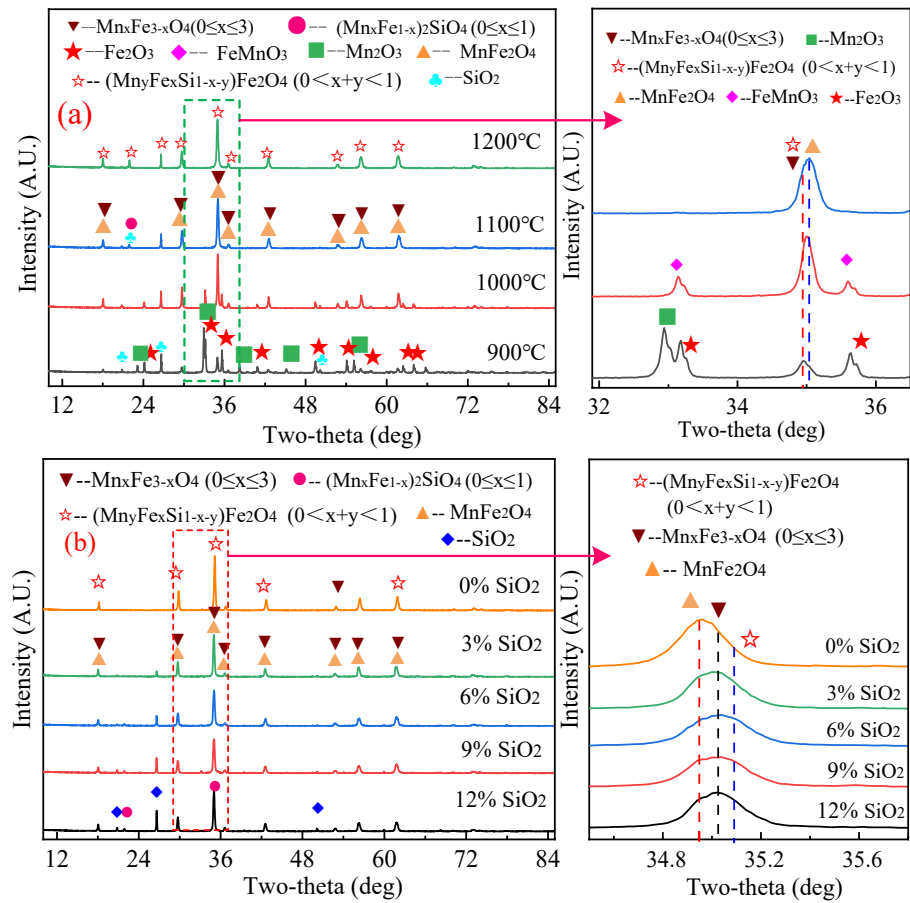


Figure 6. XRD patterns of $MnFe_2O_4$ samples calcined in $MnO-Fe_2O_3-SiO_2$ system in air atmosphere; (a) 900–1200 °C with 6% SiO_2 content for 60 min; (b) The different SiO_2 contents at 1100 °C for 60 min.

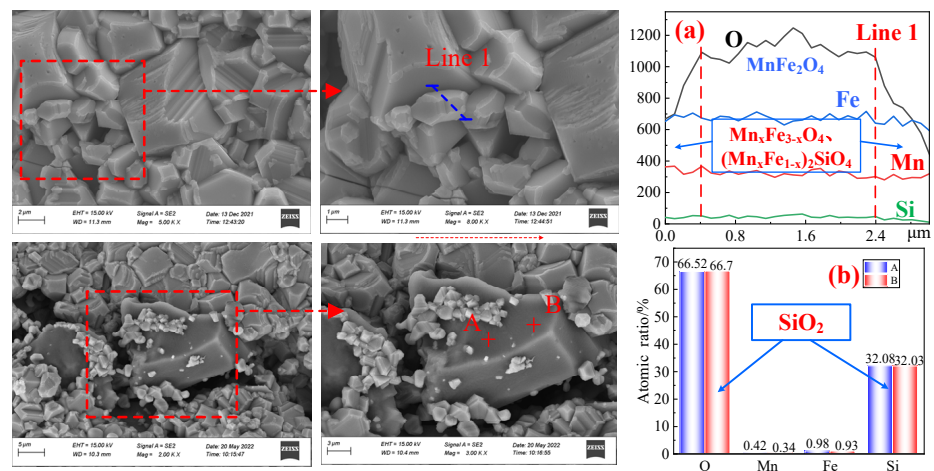


Figure 7. SEM-EDS micrograph of the surface layer in the section of the synthetic manganese ferrite samples in air atmosphere, (a) Samples roasted at 1100 °C for 60 min, (b) Samples roasted at 1100 °C for 120 min.

3.3. Discussion on the Oxidization Behavior of $MnO-Fe_2O_3-Al_2O_3$ System

Figure 8 illustrates the XRD patterns of the $MnO-Fe_2O_3-Al_2O_3$ system at 900–1200 °C and at 1100 °C with different Al_2O_3 contents. Figure 8a shows the XRD patterns at different roasting temperatures from 900 °C to 1200 °C. The main phases detected are Mn_2O_3 , Fe_2O_3 and a small amount of $Mn_xFe_{3-x}O_4$ at 900 °C, indicating that $Mn_xFe_{3-x}O_4$ is not easily

synthesized by Mn_2O_3 and Fe_2O_3 at low temperatures. Al was present in the form of Al_2O_3 , and other than a small amount of Al_2O_3 characteristic peaks, no other forms of characteristic peaks were obviously identified. As the roasting temperature increases from 900°C to 1100°C , the diffraction peaks of Mn_2O_3 and Fe_2O_3 disappear, and the intensity of the characteristic peak of $\text{Mn}_x\text{Fe}_{3-x}\text{O}_4$ increases continuously. The intensity of the characteristic peak of $\text{Mn}_x\text{Fe}_{3-x}\text{O}_4$ increases continuously and moves toward the main characteristic peak of MnFe_2O_4 (PDF#10-0319) at $2\theta = 34.981^\circ$. When the temperature increases from 1000°C to 1100°C , the diffraction peak of MnFe_2O_4 shifts from $2\theta = 34.921^\circ$ to $2\theta = 35.176^\circ$. At the same time, the presence of spinel phases $\text{Mn}_y(\text{Fe}_{3-y-z}\text{Al}_z)\text{O}_4$ and Fe_xO_4 were detected, however in small amounts. The above results indicate, on one hand, that some $\text{Mn}_x\text{Fe}_{3-x}\text{O}_4$ was converted to $\text{Mn}_y(\text{Fe}_{3-y-z}\text{Al}_z)\text{O}_4$ due to the continuous entry of some Al ions into the spinel-type manganese ferrite lattice to occupy the octahedral B-site during the reaction [35]. On the other hand, it demonstrates that the oxides of Fe ions replaced by Al ions were decomposed at high temperatures to form some low-valent Fe-oxides, leading to an increase of Fe-oxides Fe_xO_4 in the material phase. Figure 8b shows the XRD patterns of Al_2O_3 with different contents roasted at 1100°C for 120 min in the $\text{MnO-Fe}_2\text{O}_3\text{-Al}_2\text{O}_3$ system. The diffraction peaks of $\text{Mn}_x\text{Fe}_{3-x}\text{O}_4$, MnFe_2O_4 and $\text{Mn}_y(\text{Fe}_{3-y-z}\text{Al}_z)\text{O}_4$ were detected from Figure 8b, whereas the diffraction peaks of Mn_2O_3 and Fe_2O_3 were not detected. This demonstrates that the content of Al_2O_3 has less influence on the reaction process of MnO and Fe_2O_3 under the experimental conditions. The position of the characteristic peak (3 1 1) of $\text{Mn}_x\text{Fe}_{3-x}\text{O}_4$ shifts from $2\theta = 35.06^\circ$ to $2\theta = 35.241^\circ$ with increasing Al_2O_3 content, and the characteristic peaks of Fe_xO_4 and $\text{Mn}_y(\text{Fe}_{3-y-z}\text{Al}_z)\text{O}_4$ are detected. This indicates that the amount of high content of Al_2O_3 in the spinel phase increases at 1100°C and increases the decomposition of iron high-valent oxidation.

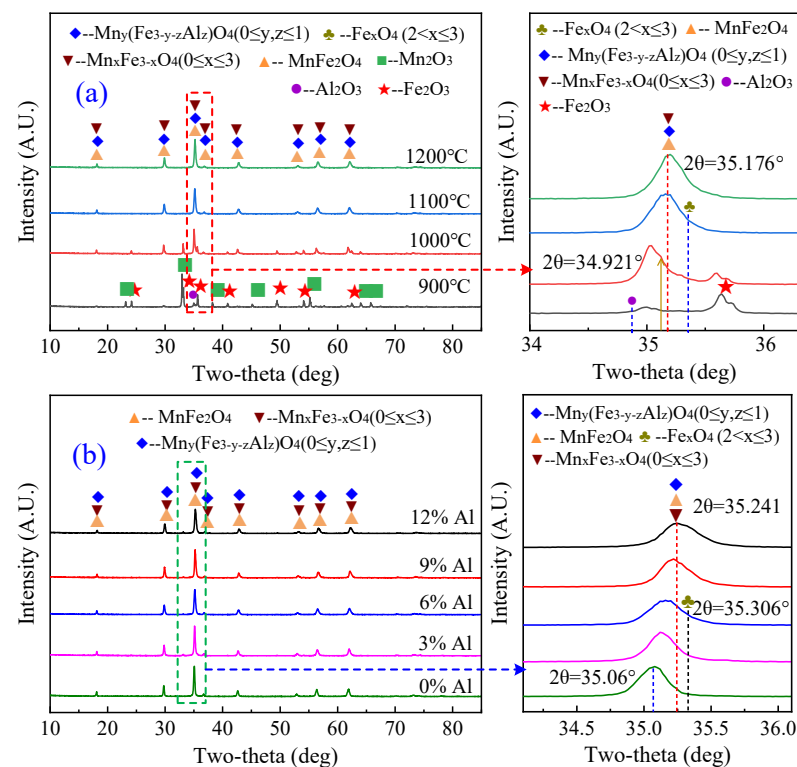


Figure 8. XRD patterns of MnFe_2O_4 samples calcined in $\text{MnO-Fe}_2\text{O}_3\text{-Al}_2\text{O}_3$ system in air atmosphere; (a) XRD patterns of MnFe_2O_4 samples with a MnO to Fe_2O_3 ratio of 1:1 and the Al_2O_3 mass fraction of 6% calcined at $900\sim 1200^\circ\text{C}$ for 60 min; (b) XRD patterns of different Al_2O_3 contents roasted at 1100°C for 60 min.

Figure 9 displays the SEM image of the cross-sectional layers of the sample roasted at 1100 °C with a mass content of 6% Al₂O₃. It can be clearly seen that the synthesized sample presents a regular polyhedral structure with a relatively uniform distribution. There are obvious boundaries between the particles, and the morphology of individual particles is mainly flat and spherical. The results obtained by the energy spectral line scan of the physical phase are shown in Figure 9b, which illustrates that the O, Fe and Mn contents are basically stable and the contents are close to 4:2:1, indicating that the composition of the synthesized sample is relatively pure. Combined with the analysis in Figure 9b, only a very small amount of Mn_y(Fe_{3-y-z}Al_z)O₄ was present, which further proves the slow solid-phase reaction of Al₂O₃ with manganese and iron oxides. From Figure 9a, it is found that the contents of Fe and Mn at different positions are relatively evenly distributed, showing an overall ratio of 2:1. There is an obvious gradient of Al, which indicates that Al₂O₃ enters the spinel-type manganese ferrite more slowly. In summary, the presence of a low content of Al₂O₃ in the MnO-Fe₂O₃ system has less effect on manganese ferrite, but a synthesis temperature above 1100 °C and Al₂O₃ content above 6% will promote the conversion of Mn_xFe_{3-x}O₄ to Mn_y(Fe_{3-y-z}Al_z)O₄. This led to a decrease in the amount of manganese ferrite produced, which in turn affected the purity of the product.

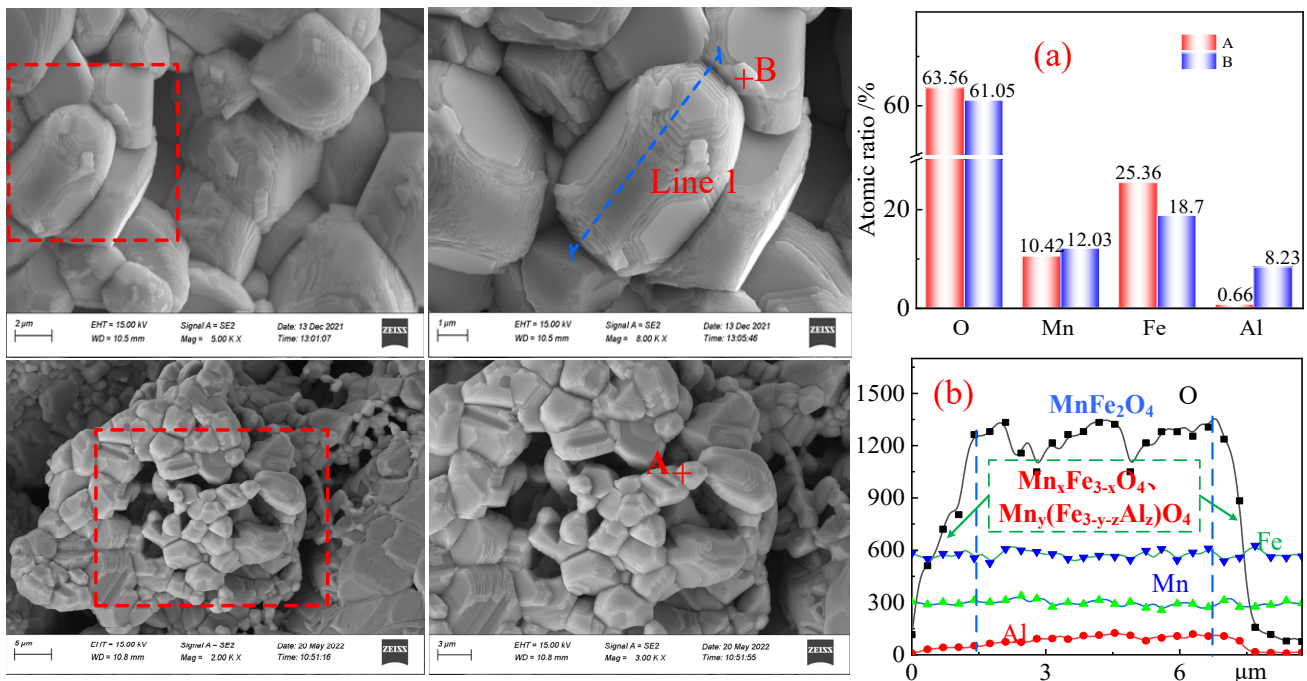


Figure 9. SEM-EDS micrograph of the surface layer in the section of the synthetic manganese ferrite samples in air atmosphere, (a) Samples roasted at 1100 °C for 60 min, (b) Samples roasted at 1100 for 120 min.

3.4. Oxidative Competition Behavior and Formation Mechanism in Synthesis Process of MnFe₂O₄

Based on the abovementioned results and analysis, the schematic diagram for preparation is illustrated in Figure 10a during the oxidative roasting process. In summary, the three stages were roughly divided for synthesizing manganese ferrite MnFe₂O₄ in Equations (1)–(7). In the initial stages (Equations (1)–(3)), magnetite (Fe)_x[Fe]₂O₄ (0.878 ≤ x ≤ 1) was easily oxidized to hematite, which contained both hexagonal and cubic crystal structures. The existence of magnetite (Fe)_x[Fe]₂O₄ and maghemite γ-Fe₂O₃ have a spinel-type crystal structure with a face-center cubic (FCC) configuration, in which both of them combine with MnO to form (Mn_xFe_{1-x})Fe₂O₄ (0 ≤ x ≤ 1) with a similar crystal structure [38,39]. Primarily because the tetrahedral Fe²⁺ ions in magnetite were partially replaced by octahedral Fe³⁺ ions, the octahedral coordination occupied by the Fe²⁺ ions generated vacancies, providing an advan-

tageous environment for the Mn^{2+} ions to form $(\text{Mn}_x\text{Fe}_{1-x})\text{Fe}_2\text{O}_4$ ($0 \leq x \leq 1$) during the oxidation roasting process of converting from magnetite to maghemite. In the second stage (Equations (4)–(6)), the replaced Fe^{2+} ions were directly oxidized to Fe^{3+} ions, while the other Fe^{2+} ions combined with Mn^{2+} ions to form an intermediate wustite phase $(\text{Mn}_y\text{Fe}_{1-y})\text{O}$, which was ultimately oxidized to $(\text{Mn}_x\text{Fe}_{1-x})\text{Fe}_2\text{O}_4$ ($0 \leq x \leq 1$). In the final stage (Equation (7)), $(\text{Mn}_x\text{Fe}_{1-x})\text{Fe}_2\text{O}_4$ ($0 \leq x \leq 1$) was characterized as $(\text{Mn}_{1-\alpha}\text{Fe}_\alpha)_{\text{tet}}[\text{Mn}_\alpha\text{Fe}_{2-\alpha}]_{\text{oct}}\text{O}_4$ ($0 \leq \alpha \leq 1$) with the face-centered cubic (FCC) structure of the spinel crystal structure, where α is called the inversion parameter [40,41]. The higher temperature and oxidation environment promoted the mutual transformation between the normal and inverse spinel structure, in which the vacancy requirements for the oxidation reaction were not easily provided during this process, thereby inhibiting the recrystallization process of pellets, resulting in lower metallurgical properties of magnesia flux pellets.

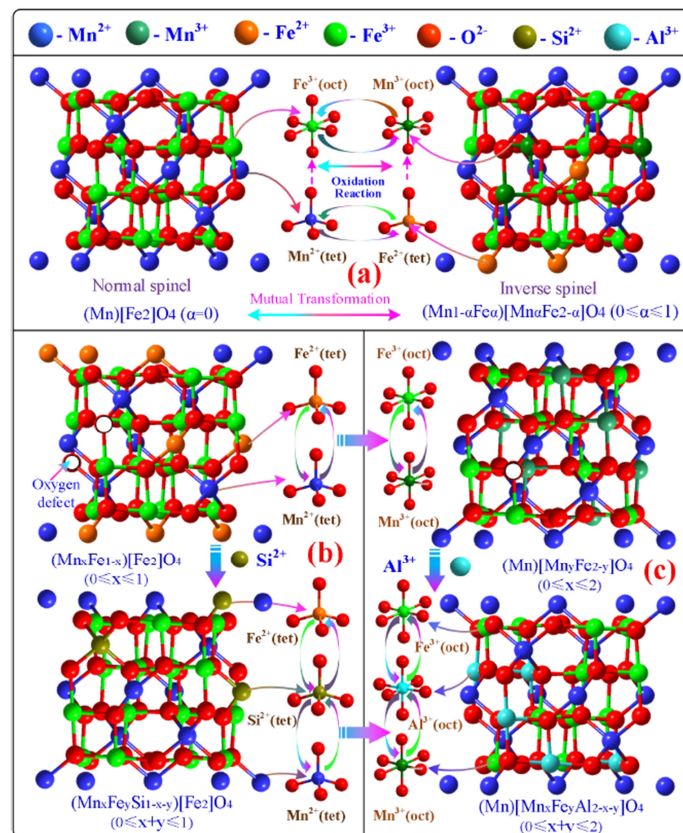
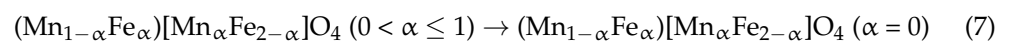
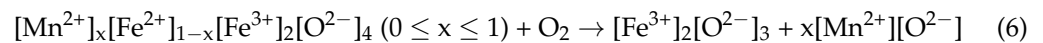
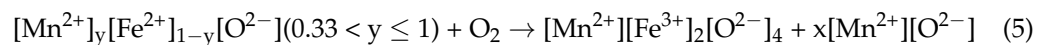
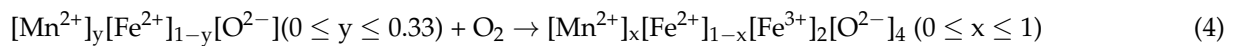
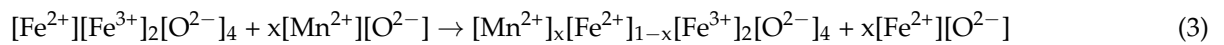
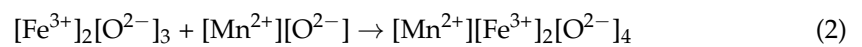
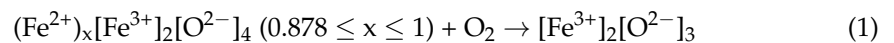
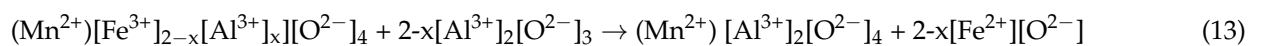
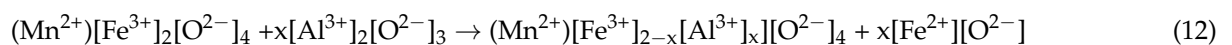
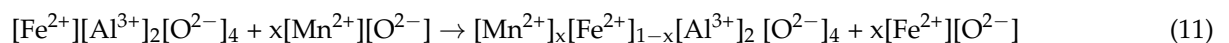
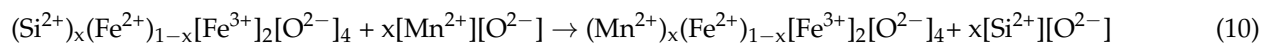
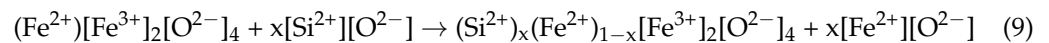
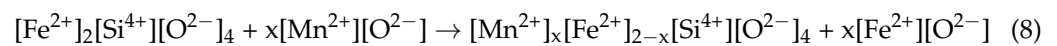


Figure 10. Schematic diagram of phase transformation mechanism and oxidation behavior in synthesizing process of manganese ferrite MnFe_2O_4 , (a) Fe_2O_3 - MnO system, (b) Fe_2O_3 - MnO - SiO_2 system and (c) Fe_2O_3 - MnO - Al_2O_3 system.

The schematic diagram for the effect of Si on synthesizing manganese ferrite MnFe_2O_4 is illustrated in Figure 10b during the oxidative roasting process. The two stages in Equations (8)–(10) were roughly divided for synthesizing manganese ferrite MnFe_2O_4 during the oxidative roasting process. In the initial stages (Equation (8)), these crystal structures of olivine-type Fe_2SiO_4 and $\text{Mn}_x\text{Fe}_{2-x}\text{SiO}_4$ had similar olivine-type crystal structures. The Fe^{2+} ions in olivine Fe_2SiO_4 are easily replaced by Mn^{2+} ions to form olivine $\text{Mn}_x\text{Fe}_{2-x}\text{SiO}_4$, in which a portion of the replaced Mn^{2+} ions and Fe^{2+} ions combine from wustite ($\text{Mn}_x\text{Fe}_{1-x}\text{O}$), and another portion of the replaced Fe^{2+} ions is directly oxidized to $\text{Mn}_x\text{Fe}_{3-x}\text{O}_4$ ($0 \leq x \leq 3$). In the second stage (Equations (9)–(10)), it is worth noting that the formation of $(\text{Fe}_x\text{Si}_{1-x})\text{Fe}_2\text{O}_4$ mainly originated from $(\text{Mn}_x\text{Fe}_{1-x})\text{Fe}_2\text{O}_4$, in which the tetrahedral Fe^{2+} ions and Mn^{2+} in the crystal structure of magnetite were replaced by tetrahedral Si^{2+} ions in the crystal structure of silicates to form $(\text{Fe}_x\text{Si}_{1-x})\text{Fe}_2\text{O}_4$ under higher oxidization roasting temperatures and the presence of SiO_2 .

The schematic diagram for the effect of Al on synthesizing manganese ferrite MnFe_2O_4 is illustrated in Figure 10c. The two stages in Equations (11)–(13) were roughly divided for synthesizing manganese ferrite MnFe_2O_4 . In the initial stages, the crystal structures of hercynite FeAl_2O_4 and $\text{Fe}_x\text{Mn}_{1-x}\text{Al}_2\text{O}_4$ were similar. Some of the Fe^{2+} ions in hercynite FeAl_2O_4 are easily replaced by Mn^{2+} ions to form hercynite $\text{Fe}_x\text{Mn}_{1-x}\text{Al}_2\text{O}_4$ ($0 \leq x \leq 1$) and further form MnAl_2O_4 after the displacement reaction. In the second stage (Equations (12)–(13)), the formation of $(\text{Mn}^{2+})[\text{Fe}^{3+}]_{2-x}[\text{Al}^{3+}]_x\text{O}_4$ mainly originated from $(\text{Mn}^{2+})[\text{Fe}^{3+}]_2\text{O}_4$, in which the octahedral Fe^{3+} ions and octahedral Mn^{3+} ions in the crystal structure of manganese ferrite MnFe_2O_4 were replaced by octahedral Al^{3+} ions to form $(\text{Mn}^{2+})[\text{Fe}^{3+}]_{2-x}[\text{Al}^{3+}]_x\text{O}_4$ under higher oxidization roasting temperatures and the presence of Al_2O_3 . In summary, the tetrahedral Mn^{2+} ions and octahedral Mn^{3+} ions in the crystal structure of manganese ferrite MnFe_2O_4 were replaced by tetrahedral Si^{2+} ions and octahedral Al^{3+} ions from $(\text{Mn}^{2+})_x(\text{Fe}^{2+})_y(\text{Si}^{2+})_{1-x-y}[\text{Fe}^{3+}]_2\text{O}_4$ and $(\text{Mn}^{2+})[\text{Fe}^{3+}]_{2-x}[\text{Al}^{3+}]_x\text{O}_4$, respectively.



4. Conclusions and Future Prospects

In this work, a new understanding of the synthesis and magnetism properties of manganese ferrite MnFe_2O_4 with a spinel crystal structure was proposed to elucidate the oxidization behavior and consolidation mechanism in the oxidization roasting process. The synthetic MnFe_2O_4 polyhedral microparticle samples with a saturated magnetization of 71.19 emu/g, a ratio of the saturation magnetization to residual magnetization (M_s/M_r) of 0.062 and a coercivity (H_c) of 6.50 Oe can be successfully obtained at an oxidization roasting temperature of 1100 °C for 60 min in the $\text{MnO-Fe}_2\text{O}_3$ system.

This work clarified the underlying reason for the influence mechanism of SiO_2 and Al_2O_3 on the synthesis of MnFe_2O_4 . The experimental results indicate that the tetrahedral Mn^{2+} ions and octahedral Mn^{3+} ions in the crystal structure of manganese ferrite MnFe_2O_4 were replaced by tetrahedral Si^{2+} ions and octahedral Al^{3+} ions from $(\text{Mn}^{2+})_x(\text{Fe}^{2+})_y(\text{Si}^{2+})_{1-x-y}[\text{Fe}^{3+}]_2\text{O}_4$ and $(\text{Mn}^{2+})[\text{Fe}^{3+}]_{2-x}[\text{Al}^{3+}]_x\text{O}_4$, respectively. In addition, hercynite $\text{Fe}_x\text{Mn}_{1-x}\text{Al}_2\text{O}_4$ with a

spinel crystal structure and olivine $Mn_xFe_{2-x}SiO_4$ with an orthorhombic crystal structure were partially formed in the synthesis of manganese ferrite $MnFe_2O_4$, in which some Fe^{2+} ions were easily replaced by Mn^{2+} ions to form stable hercynite $MnAl_2O_4$ and olivine Mn_2SiO_4 in these crystal structures. The current research work provides comprehensive insights for synthesizing manganese ferrite $MnFe_2O_4$ and continuously advances its technical progress.

Author Contributions: S.W.: Writing—review & editing, Methodology. B.C.: Methodology, Funding acquisition. J.Z.: Funding acquisition, Methodology, Investigation, Visualization. W.Z.: Software, Funding acquisition. Z.H.: Methodology, Funding acquisition. L.G.: Writing—original draft, Methodology, Funding acquisition. All authors have read and agreed to the published version of the manuscript.

Funding: The work was supported by Doctoral research Foundation of Liaoning Province (2023-BS-181), National Natural Science Foundation of China (52104332, 52074150, 52374339), University of Science and Technology Liaoning Talent Project Grants (601011507-05).

Data Availability Statement: Not applicable.

Acknowledgments: The authors especially thank Y. Liang, H.Y. Sheng and X.Y. Yi for their help in this work.

Conflicts of Interest: The authors declare no conflict of interest.

References

1. Liu, F.; Liu, J.; Yang, Y.; Wang, X. A mechanistic study of CO oxidation over spinel $MnFe_2O_4$ surface during chemical-looping combustion. *Fuel* **2018**, *230*, 410–417. [CrossRef]
2. Guo, W.; Zhu, H.; Ren, Q.; Chen, S.; Ding, Y.; Xiong, C.; Chen, J.; Jia, X. $MnFe_2O_4/ZnO$ /diatomite composites with electromagnetic wave absorption and antibacterial bifunctions. *Solid State Sci.* **2023**, *138*, 107152. [CrossRef]
3. Mounkachi, O.; Lamouri, R.; Salmani, E.; Hamedoun, M.; Benyoussef, A.; Ez-Zahraouy, H. Origin of the magnetic properties of $MnFe_2O_4$ spinel ferrite: Ab initio and Monte Carlo simulation. *J. Magn. Magn. Mater.* **2021**, *533*, 168016. [CrossRef]
4. Qian, Z.; Ting, Y.; Guo, G.; Shapter, G.J.; Lai, W.E.; Huang, P.; Qi, W.; Song, J.; Cui, D.X. Multifunctional Core@Shell Magnetic Nanoprobes for Enhancing Targeted Magnetic Resonance Imaging and Fluorescent Labeling In Vitro and In Vivo. *J. Appl. Mater. Interfaces* **2017**, *21*, 17777–17785.
5. Martin, L.; Stigler, J.; Elia, G.; Lynch, I.; Tommy, C.; Dawson, A.K. Nanoparticle size and surface properties determine the protein corona with possible implications for biological impacts. *Appl. Surf. Sci.* **2008**, *38*, 14265–14270.
6. Marcela, S.; Eliza, M.; Cornelia, P.; Ciprian, M. Thermal behavior of $MnFe_2O_4$ and $MnFe_2O_4/C$ nanocomposite synthesized by a solvothermal method. *Thermochim. Acta* **2017**, *652*, 1–8.
7. Peng, E.; Choo, E.S.G.; Chandrasekharan, P.; Yang, C.; Ding, J.; Chuang, K.; Xue, J.M. Synthesis of manganese ferrite/graphene oxide nanocomposites for biomedical applications. *Small* **2012**, *8*, 3620–3630. [CrossRef]
8. Rajalakshmi, R.; Ponpandian, N. Morphological design of $MnFe_2O_4$ facets (cube, flakes and capsules) for their role in electrical, magnetic and photocatalytic activity. *Mater. Res. Bull.* **2023**, *164*, 112242. [CrossRef]
9. Wu, X.F.; Ding, Z.; Wang, W.; Song, N.N.; Khaimanov, S.; Tsiadaeva, N. Effect of polyacrylic acid addition on structure, magnetic and adsorption properties of manganese ferrite nanoparticles. *Powder Technol.* **2016**, *295*, 59–68. [CrossRef]
10. Mondal, D.K.; Borgohain, C.; Paul, N.; Borah, J.P. Tuning hyperthermia efficiency of $MnFe_2O_4/ZnS$ nanocomposites by controlled ZnS concentration. *J. Mater. Res. Technol.* **2019**, *8*, 5659–5670. [CrossRef]
11. Neda, A.; Ghasem, N. A Manganese ferrite ($MnFe_2O_4$) Nanoparticles: From synthesis to application—A review. *J. Ind. Eng. Chem.* **2021**, *103*, 292–304.
12. Masrour, R. Magnetic properties of the spinel systems ACr_2X_4 ($A = Zn, Cd, Hg; X = S, Se$). *J. Alloys Compd.* **2010**, *489*, 441–444. [CrossRef]
13. Leal, M.P.; Rivera-Fernández, S.; Franco, J.M. Long-circulating PEGylated manganese ferrite nanoparticles for MRI-based molecular imaging. *Nanoscale* **2015**, *7*, 2050–2059. [CrossRef] [PubMed]
14. Misra, R.D.K.; Gubbala, S.; Kale, A.; Egelhoff, W.F.E., Jr. A comparison of the magnetic characteristics of nanocrystalline nickel, zinc, and manganese ferrites synthesized by reverse micelle technique. *Mater. Sci. Eng. B* **2004**, *111*, 164–174. [CrossRef]
15. Lin, X.M.; Lv, X.; Wang, L.M.; Zhang, F.F.; Duan, L.F. Preparation and characterization of $MnFe_2O_4$ in the solvothermal process: Their magnetism and electrochemical properties. *Mater. Res. Bull.* **2013**, *48*, 2511–2516. [CrossRef]
16. Carpenter, E.E.; O'Connor, C.J.; Harris, V.G. Atomic structure and magnetic properties of $MnFe_2O_4$ nanoparticles produced by reverse micelle synthesis. *J. Appl. Phys.* **1999**, *85*, 5175–5177. [CrossRef]
17. Lazarova, T.; Kovacheva, D.; Georgieva, M.; Tzankov, D.; Tyuliev, G.; Spassova, I.; Naydenov, A. Tunable nanosized spinel manganese ferrites synthesized by solution combustion method. *Appl. Surf. Sci.* **2019**, *496*, 143571. [CrossRef]

18. Liu, B.B.; Zhang, Y.B.; Su, Z.J.; Lu, M.M.; Peng, Z.W.; Li, G.H.; Jiang, T. Formation mechanism of $Mn_xFe_{3-x}O_4$ by solid-state reaction of MnO_2 and Fe_2O_3 in air atmosphere Morphologies and properties evolution. *Powder Technol.* **2017**, *313*, 201–209. [[CrossRef](#)]
19. Ahmad, S.; Ali, S.; Ullah, I.; Zobaer, M.S.; Albakri, A.; Muhammad, T. Synthesis and characterization of manganese ferrite from low grade manganese ore through solid state reaction route. *Sci. Rep.* **2021**, *11*, 16190. [[CrossRef](#)]
20. Liu, B.B.; Zhang, Y.B.; Wang, J.; Wang, J.; Su, Z.J.; Li, G.H.; Jiang, T. A further investigation on the MnO_2 - Fe_2O_3 system roasted under CO-CO₂ atmosphere. *Adv. Powder Technol.* **2019**, *30*, 302–310. [[CrossRef](#)]
21. Wang, G.; Zhao, D.; Ma, Y.; Zhang, Z.; Che, H.; Mu, J.; Zhang, X.; Zhang, Z. Synthesis and characterization of polymer-coated manganese ferrite nanoparticles as controlled drug delivery. *Appl. Surf. Sci.* **2018**, *428*, 258–263. [[CrossRef](#)]
22. Reddy, M.P.; Mohamed, A.M.A.; Raman, M.V.; Zhou, X.B.; Huang, Q. Spark plasma sintering and microwave electromagnetic properties of $MnFe_2O_4$ ceramics. *J. Magn. Magn. Mater.* **2015**, *395*, 185–189. [[CrossRef](#)]
23. Rashad, M.M. Synthesis and magnetic properties of manganese ferrite from low grade manganese ore. *Mater. Sci. Eng. B* **2006**, *127*, 123–129. [[CrossRef](#)]
24. Ahmed, Y.M.Z. Synthesis of manganese ferrite from non-standard raw materials using ceramic technique. *Ceram. Int.* **2010**, *36*, 969–977. [[CrossRef](#)]
25. Makridis, A.; Tziomaki, M.; Topouridou, K.; Yavropoulou, M.P.; Yovos, J.G.; Kalogirou, O.; Samaras, T.; Angelakeris, M. A novel strategy combining magnetic particle hyperthermia pulses with enhanced performance binary ferrite carriers for effective in vitro manipulation of primary human osteogenic sarcoma cells. *Int. J. Hyperth.* **2016**, *32*, 778–785. [[CrossRef](#)]
26. Chen, D.; Zhang, Y.Z.; Kang, Z.T. A low temperature synthesis of $MnFe_2O_4$ nanocrystals by microwave-assisted ball-milling. *Chem. Eng. J.* **2013**, *215–216*, 235–239. [[CrossRef](#)]
27. Neda, A.; Ghasem, N.; Younesi, H. Facile and green synthesis of cobalt oxide nanoparticles using ethanolic extract of *Trigonella foenumgraceum* (Fenugreek) leaves. *Adv. Powder Technol.* **2020**, *31*, 3562–3569.
28. Aslibeiki, B.; Kameli, P. Magnetic properties of $MnFe_2O_4$ nano-aggregates dispersed in paraffin wax. *J. Magn. Magn. Mater.* **2015**, *385*, 308–312. [[CrossRef](#)]
29. Ba-Abbad, M.M.; Chai, P.V.; Takriff, M.S.; Benamor, A.; Mohammad, A.W. Optimization of nickel oxide nanoparticle synthesis through the sol-gel method using Box-Behnken design. *Mater. Des.* **2015**, *86*, 948–956. [[CrossRef](#)]
30. Yan, Z.; Chaluvadi, A.; FitzGerald, S.; Spence, S.; Bleyer, C.; Zhu, J.; Crawford, T.M.; Getman, R.B.; Watt, J.; Huber, D.L.; et al. Effect of manganese substitution of ferrite nanoparticles on particle grain structure. *Nanoscale Adv.* **2022**, *4*, 3957–3965. [[CrossRef](#)]
31. Gao, L.H.; Liu, Z.G.; Ge, Y.; Feng, C.; Chu, M.S.; Tang, J. Synthesis and characterization of manganese ferrite $Mn_xFe_{3-x}O_4$ from ferruginous manganese ores by multi-step roasting and magnetic separation. *Powder Technol.* **2019**, *356*, 373–382. [[CrossRef](#)]
32. Devan, R.S.; Ma, Y.; Chougule, B.K. Effective dielectric and magnetic properties of (Ni-Co-Cu) ferrite/BTO composites. *Mater. Chem. Phys.* **2009**, *115*, 263–268. [[CrossRef](#)]
33. Shekhar, D.B.; Pattayil, A.J. Effect of sintering conditions and microstructure on the magnetostrictive properties of cobalt ferrite. *J. Am. Ceram. Soc.* **2008**, *91*, 1976–1980.
34. Gao, L.H.; Liu, Z.G.; Yang, Z.C.; Feng, L.G.C.; Chu, M.S.; Tang, J. Synthesis and magnetism property of manganese ferrite $MnFe_2O_4$ by selective reduction and oxidization roasting process. *Appl. Surf. Sci.* **2020**, *508*, 145292–145301. [[CrossRef](#)]
35. Zhao, X.R.; Wang, W.; Zhang, Y.J.; Wu, S.Z.; Li, F.; Liu, J.P. Synthesis and characterization of gadolinium doped cobalt ferrite nanoparticles with enhanced adsorption capability for Congo Red. *Chem. Eng. J.* **2014**, *250*, 164–174. [[CrossRef](#)]
36. Wang, Z.; Chen, H.; Han, X.; Gao, L.; Zhan, W.; Zhang, J.; He, Z. Preparation and characterization of $MnFe_2O_4$ by a microwave-assisted oxidative roasting process. *Adv. Powder Technol.* **2023**, *34*, 104040. [[CrossRef](#)]
37. Šepelák, V.; Baabe, D.; Mienert, D.; Schultze, D.; Krumeich, F.; Litterst, F.J.; Becker, K.D. Evolution of structure and magnetic properties with annealing temperature in nanoscale high-energy-milled nickel ferrite. *J. Magn. Magn. Mater.* **2003**, *257*, 377–386. [[CrossRef](#)]
38. Gao, L.H.; Liu, P.; Zhan, W.L.; Zhang, J.H.; He, Z.J.; Hou, X. New understanding on formation mechanism of $CaFe_2O_4$ in Fe_2O_3 - Fe_3O_4 - CaO - SiO_2 system during sintering Process: Phase transformation and morphologies evolution. *Adv. Powder Technol.* **2022**, *33*, 103712. [[CrossRef](#)]
39. Cheng, F.Y.; Shen, J.; Peng, B.; Pan, Y.D.; Tao, Z.L.; Chen, J. Rapid room-temperature synthesis of nanocrystalline spinels as oxygen reduction and evolution electrocatalysts. *Nat. Chem.* **2011**, *3*, 79–84. [[CrossRef](#)]
40. Allen, G.C.; Hallam, K.R. Characterisation of the spinels $M_xCo_{1-x}Fe_2O_4$ (M=Mn, Fe or Ni) using X-ray photoelectron spectroscopy. *Appl. Surf. Sci.* **1996**, *93*, 25–30. [[CrossRef](#)]
41. Mirza, M.; Muhammad, A.; Philips, O.; Muhammad, A.; Imran, S.; Muhammad, F. Optimization of different wet chemical routes and phase evolution studies of $MnFe_2O_4$ nanoparticles. *Ceram. Int.* **2019**, *45*, 12682–12690.

Disclaimer/Publisher’s Note: The statements, opinions and data contained in all publications are solely those of the individual author(s) and contributor(s) and not of MDPI and/or the editor(s). MDPI and/or the editor(s) disclaim responsibility for any injury to people or property resulting from any ideas, methods, instructions or products referred to in the content.